Numerical investigation of ventilated cavitating flow in the wake of a circular cylinder

Zhiying Wang,[1,2,*] Han Liu,[3,4] Qiang Gao,[3,4] Zhan Wang,[1,2] Yiwei Wang,[1,2] Guoyu Wang,[5] and Lian Shen[3,4]

[1]*Key Laboratory for Mechanics in Fluid Solid Coupling Systems, Institute of Mechanics, Beijing, 100190, China*

[2]*School of Engineering Science, University of Chinese Academy of Sciences, Beijing, 100049, China*

[3]*Department of Mechanical Engineering, University of Minnesota, Minneapolis, Minnesota 55414, USA*

[4]*Saint Anthony Falls Laboratory, University of Minnesota, Minneapolis, Minnesota 55455, USA*

[5]*School of Mechanical and Vechicular Engineering, Beijing Institute of Technology, Beijing, 100081, China*

(Received 19 December 2020; accepted 17 May 2021; published 8 June 2021)

Ventilated cavitating flow of a circular cylinder is investigated by numerical simulation. The coupled level set and volume of fluid method is used to capture the interface between the cavity and surrounding water. The simulation results indicate that the bubble size distribution in the wake is closely related to the turbulence intensity. The bubble number reaches its peak value in the closure region owing to the high turbulence intensity there. When the gas entrainment coefficient Q_v increases, the length of the cavity increases and the turbulent kinetic energy decreases, leading to a decrease in the bubble number and an increase in the Sauter mean diameter. It is also found that the presence of the ventilated cavitation delays the formation of vortices and affects the vortex shedding. In the single phase flow, the enstrophy is concentrated in the shear layer and closure region. In the ventilated cavitating flow, on the other hand, the enstrophy is mainly distributed at the cavity interface and the re-entrant region, which indicates that the instability of the cavity interface and the existence of the re-entrant jet play important roles in the formation of vortices.

DOI: 10.1103/PhysRevFluids.6.064303

I. INTRODUCTION

Cavitation is a common hydrodynamic phenomenon affecting many important engineering applications, for example, spillways, propellers, and underwater vehicles. It can lead to pressure pulsation, sudden change in loads, vibration, noise, and erosion [1–3]. While cavitation can have harmful effects, it also has the benefit of reducing drag on a body when the cavity size is large enough to encompass the body, a phenomenon called supercavitation. Supercavitation is among the most promising techniques for skin friction reduction of underwater vehicles. It can be classified into two categories: vaporous supercavitation, which can be achieved if the speed of the vehicle is sufficiently high, and ventilated supercavitation, which is achieved through artificial injection of air or a noncondensable gas [4]. Ventilated supercavitation is often considered in practice because it can occur at relatively low speeds [5]. There have been many studies on ventilated supercavitation using experimental and numerical methods [6–10]. Cavitation often experiences unsteady behaviors (partial cavitation) before supercavitation can be achieved. There exist a variety of cavitation topologies, such as sheet, cloud, and vortex cavitations. Partial cavitation, which is

*wangzhiying@imech.ac.cn

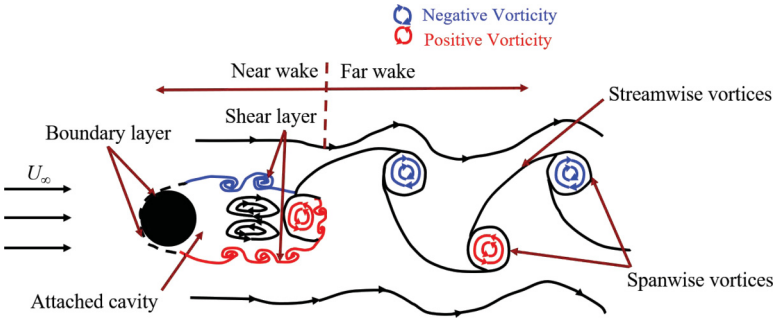

FIG. 1. Schematic of cavitating flow over a bluff body.

associated with the vortex shedding phenomenon, is a research topic of great interest in the literature [11–15]. Callenaere *et al.* [16] pointed out that the development of a re-entrant jet plays an important role in the stability of partial cavitation. The instability of a re-entrant jet is related to the adverse pressure gradient and the cavity thickness. Ji *et al.* [17] examined the cavitation structure and vortex shedding dynamics around a NACA66 hydrofoil numerically. Harwood *et al.* [18] performed a series of experiments to study the formation, instability, and diminution of ventilated cavities on a surface-piercing hydrofoil. The results indicated that the stability of a ventilated cavity is related to the angle of the re-entrant jet.

While the unsteady behavior of cavitation, including vaporous cavitation and ventilated cavitation, has been widely studied, there have been relatively fewer studies related to bluff bodies [19–22]. The flow over a bluff body possesses complexities unique due to the flow separation, especially in multiphase flow [23–26]. As shown in Fig. 1, the turbulent wake of cavitating flow over a circular cylinder can be divided into two parts: a near wake and a far wake. In the near wake, there exist a boundary layer, a shear layer, and a ventilated cavity. The flow in the near wake is characterized by the cavity/boundary layer interaction, cavity interfacial instabilities, laminar-to-turbulent transition, development of multiscale vortices, and re-entrant jet formation. In the far wake, the alternating shedding of vortices results in the formation of a vortex street. Belahadji *et al.* [27] showed the existence of three kinds of rotational structures in a cavitating turbulent wake, namely the primary spanwise vortices, secondary streamwise vortices, and near-wake vortices. They found that cavitation played an important role in determining the value of the Strouhal number and in the mechanism of vortex shedding. Brander *et al.* [28] conducted a series of experiments to investigate cavitation over a sphere, especially cloud cavitation. They found that when the cavitation number was around 0.95, the cavity length allowed the development of a re-entrant jet, which played an important role in cavity breakup. They also illustrated the complex interaction between the boundary layer and the detaching cavity. Because cavitation involves large variations in the fluid density and pressure fluctuations, the various limitations of measurement techniques have led to the increasing use of numerical simulations. Gnanaskandan and Mahesh [29] applied large-eddy simulation (LES) to investigate the characteristics of cavitating flow over a circular cylinder at $\mathrm{Re} = 200$ and 3900 (Re is based on the diameter and free-stream velocity). Their results demonstrated that cavitation had an influence on the evolution of the pressure, the boundary layer, and the loads on the cylinder surface. In addition, they found that cavitation suppresses turbulence and delays the three-dimensional breakdown of Kármán vortices. The studies reviewed above indicate that cavitation makes the flow physics in the turbulent wake behind a bluff body more complex. However, except for a few aspects revealed in some studies, the characteristics of ventilated cavitating flow over a bluff body are not well understood.

Ventilated cavitation is a typical multiphase flow, and the property of the cavity interface has a significant effect on the amount of air entrained and the internal flow field [30]. To capture the interface, an interface capture method is needed, which includes but is not limited to the

volume of fluid (VOF) method [31,32], the level-set method (LS) [33], and coupled LS and VOF method [34]. Kim and Lee [35] used the VOF method to track the cavity interface to study the effect of hydrophobicity on cloud cavitation. Their results showed that the instability of the cloud cavitation was alleviated when the hydrophobicity increased. Penda and Roohi [36] investigated the characteristics of partial cavitation and supercavitation over a sphere using the VOF method. They found that cavitation could effectively suppress turbulence. The VOF method has been widely used due to the good performance of mass conservation. However, this method sometimes leads to unexpected interface deformation due to the discontinuous spatial derivatives of the VOF function near the interface [37]. For the level-set method, accurate curvature can be obtained from the continuous and smooth distance function. It is therefore beneficial to use the coupled level-set and VOF (CLSVOF) method to capture the cavity interface, which combines the advantages of the VOF and LS methods [34,38].

In this paper, ventilated cavitating flow in the wake of a circular cylinder is studied by two-phase direct numerical simulation using an in-house finite-difference code [39,40]. The main goal is to investigate how the developed ventilated cavitation affects the bubble distribution, vortex structures, mean flow field, turbulent kinetic energy, and vortex dynamics. This paper is organized as follows. Section II introduces the numerical algorithm. Section III describes the details of problem setup and key parameters. In Sec. IV, the characteristics of ventilated cavitating flow are investigated. The conclusions are presented in Sec. V.

II. NUMERICAL METHOD

The numerical results presented in this paper are obtained by solving the water-air two-phase incompressible Navier-Stokes equations without using any turbulence models and the mass transfer is not considered here. The governing equations are

$$\frac{\partial u_i}{\partial x_i} = 0, \tag{1}$$

$$\frac{\partial u_i}{\partial t} + \frac{\partial (u_i u_j)}{\partial x_j} = -\frac{1}{\rho}\frac{\partial p}{\partial x_j} + \frac{1}{\rho}\frac{\partial \tau_{ij}}{\partial x_j} + g_i + \frac{T_i}{\rho}, \tag{2}$$

where u, p, ρ, τ, g, and T are the velocity, pressure, density, stress tensor, gravitational acceleration, and surface tension, respectively.

The continuity and momentum equations [Eqs. (1) and (2)] are spatially discretized by a second-order central difference scheme. The second-order Runge-Kutta (RK2) method is employed for time advancement, and the fractional-step method [41] is applied in each substep of the RK2 method. The pressure is solved by the Poisson equation. The details of the numerical method and its validation can be found in Ref. [39].

Ventilated cavitating flow is a multiphase flow. It is important to simulate the cavity interface accurately. As mentioned in the introduction, VOF satisfies the compliance of mass conservation extremely well and the LS method has good performance in accurate computation of normal and curvature. In this study, we used the CLSVOF method [34] to capture this interface, which combines the advantages of the VOF and LS methods. The cavity interface is obtained by the level-set method, and the VOF function is employed to correct the level-set function to enforce mass conservation.

For the level-set method [33], a signed distance function ϕ ($\phi = 0$ denotes the interface) is governed by the convection equation

$$\frac{\partial \phi}{\partial t} + u_j \frac{\partial \phi}{\partial x_j} = 0. \tag{3}$$

The VOF function F is defined as the liquid volume fraction in a cell, with a value between 0 and 1 in the surface cells. The governing equation for F is

$$\frac{\partial F}{\partial t} + u_j \frac{\partial F}{\partial x_j} = 0. \tag{4}$$

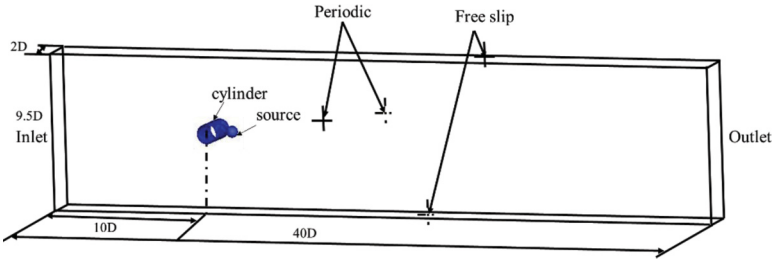

FIG. 2. Computational domain and boundary conditions.

In Eq. (2), the density and viscosity are related to the level-set function ϕ, and they can be respectively expressed as

$$\rho = \rho_a + (\rho_l - \rho_a)H(\phi), \tag{5}$$

$$\mu = \mu_a + (\mu_l - \mu_a)H(\phi), \tag{6}$$

where subscripts l and a denote the liquid and gas phases, respectively. $H(\phi)$ is a smoothed Heaviside function

$$H(\phi) = \begin{cases} 0 & \phi < -\epsilon \\ \frac{1}{2}[1 + \frac{\phi}{\epsilon} + \frac{1}{\pi}\sin(\pi\frac{\phi}{\epsilon})] & |\phi| \leqslant \epsilon \\ 1 & \phi > -\epsilon \end{cases}, \tag{7}$$

where ϵ is half the interface's numerical thickness.

In this method, the VOF function F is used to determine the interface and ensure the mass conservation. The level-set function ϕ is used to obtain the normal direction of the interface. A piecewise linear interface calculation (PLIC) algorithm based on both F and ϕ is employed to reconstruct the interface. Then, the values ϕ near the interface are also corrected [34]. The details of our implementation of the CLSVOF method and validation tests of our code can be found in Refs. [40,42,43].

III. SIMULATION SETUP AND PARAMETERS

As shown in Fig. 2, the computational domain is $40D$ in length, $9.5D$ in height, and $2D$ in width, where D is the diameter of the circular cylinder. In the simulation, the cavitation is generated by a spherical ventilation source with a diameter of $0.6D$. It is located $1D$ behind the cylinder. The air-water density ratio is $\rho_a/\rho_w = 0.012$, and the dynamic viscosity ratio is $\mu_a/\mu_w = 0.0154$. The immersed boundary (IB) method [44] is employed to capture the cylinder on a Cartesian grid in the simulation. In the IB method, a body force term is applied at the boundary nodes near the body to enforce the nonslip boundary condition on the body surface. The details of the numerical scheme of IB method in our code, which utilizes the LS function to denote the distance to the body surface, are given in Refs. [45,46] with extensive validation tests. Free-slip boundary conditions are imposed on the top and bottom boundaries of the domain, and periodic boundary conditions are applied on the front and back boundaries. A Dirichlet boundary condition is used for the inflow, and a convective boundary condition is applied for the outflow.

IV. RESULTS

A. Bubble identification method

The ventilated cavitation internal structures are composed of many bubbles at multiple scales [47]. The bubble size distribution is related to the behavior of bubble breakup and coalescence

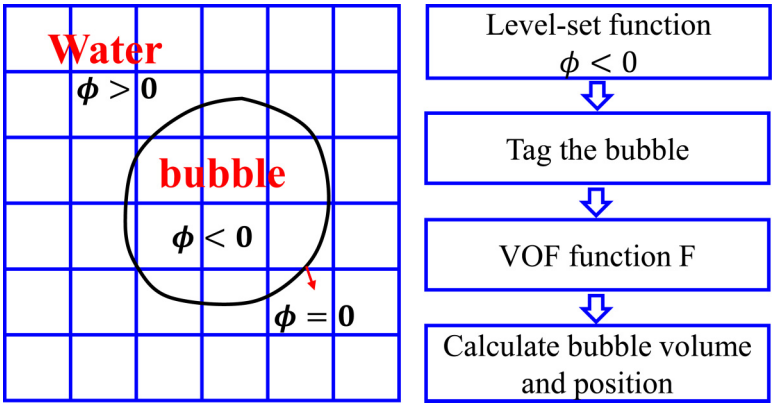

FIG. 3. Outline of the bubble identification method.

processes. To study the characteristics of the bubbles in the wake of ventilated cavitating flow, a bubble identification method [48,49] based on the level-set and VOF functions is employed to extract the quantitative information of the bubbles, including the bubble sizes, bubble number, and bubble locations. The bubble identification method is outlined in Fig. 3. The bubbles can be tracked by the level-set function ϕ. The bubble surfaces are represented by the isosurface of the zero value of the level-set function, and a bubble is identified and marked when the level-set function $\phi < 0$. The bubble information is then calculated using the following equations based on the VOF function F:

$$V_b = \sum_{bi=1}^{N_c} (1 - F_{bi}) \Delta x_i \Delta y_i \Delta z_i, \tag{8}$$

$$\overrightarrow{x_b} = \frac{1}{V_b} \sum_{bi=1}^{N_c} \overrightarrow{x_{bi}} (1 - F_{bi}) \Delta x_i \Delta y_i \Delta z_i, \tag{9}$$

where V_b is the volume of the bubble, $\overrightarrow{x_b}$ is the location of the bubble, bi denotes each of the cell marked as bubble, and N_c is the number of bubble cells.

The wake patterns and features are visible by the presence of ventilated cavitation bubbles. Figure 4 shows the instantaneous ventilated cavitation for four different values of Q_v, visualized by the isosurfaces of the gas volume fraction $\alpha_g = 0.05$ (gray) and $\alpha_g = 0.95$ (blue). The bubble coalescence and breakup behaviors in the wake at $Q_v = 0.25$ are displayed in Fig. 5. Figure 6 shows the corresponding instantaneous bubble number density distribution of bubble radius r/D versus the downstream locations x/D in the wake for four cases. The bubble number distribution function $fdrdx$ is the bubble number with location in the range of $(x, x + dx)$ and with radius in the range of $(r, r + dr)$. The color represents the bubble number density. It can be found that the bubble radius is less than $0.1D$ and the bubble number decreases with the increase of Q_v. For $Q_v = 0.1$, as shown in Fig. 4(a), a foam-ventilated cavity, which is composed of a mixture of water and gas, is attached to the circular cylinder. The gas is injected into the wake, forming a train of bubbles. From Fig. 6, it can be seen that the bubbles are mainly distributed in the closure region where bubble breakup occurs owing to the high turbulence intensity there. At the rear of the cavity, the gas is trapped at the center of the vortices. The vortices then alternately shed from the attached cavity and form a cavitation vortex street in the wake. When the gas entrainment coefficient Q_v is increased to 0.25 [Fig. 4(b)], the gas gathers to form larger bubbles. The length of the attached cavity increases, and it is large enough to allow the development of a re-entrant jet. The re-entrant jet hits the rear of the circular cylinder, and the cavity interface becomes rough and unsteady. As shown in Fig. 5, in the

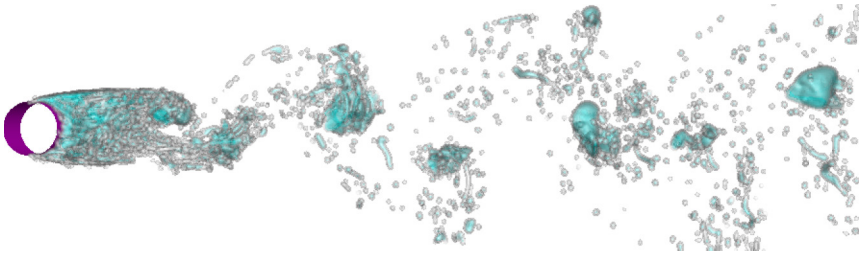

(a) $Q_v = 0.1$

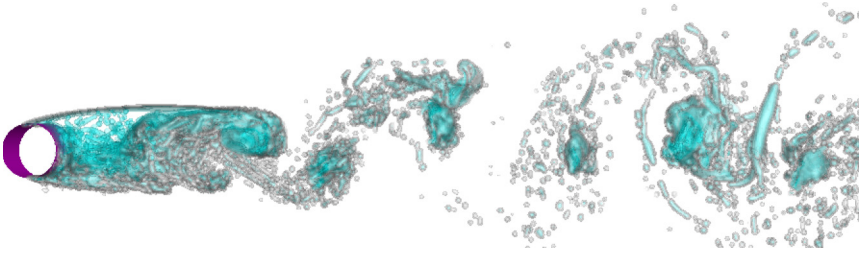

(b) $Q_v = 0.25$

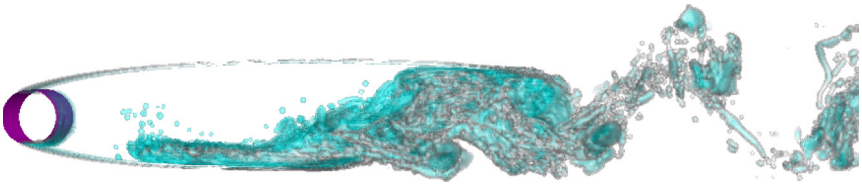

(c) $Q_v = 0.65$

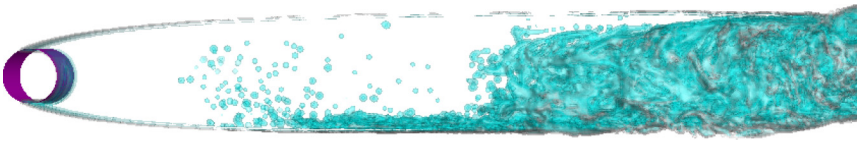

(d) $Q_v = 0.9$

FIG. 4. The isosurfaces of the gas volume fraction $\alpha_g = 0.05$ (gray) and $\alpha_g = 0.95$ (blue) over a circular cylinder at Re $= 1000$: (a) $Q_v = 0.1$, (b) $Q_v = 0.25$, (c) $Q_v = 0.65$, (d) $Q_v = 0.9$.

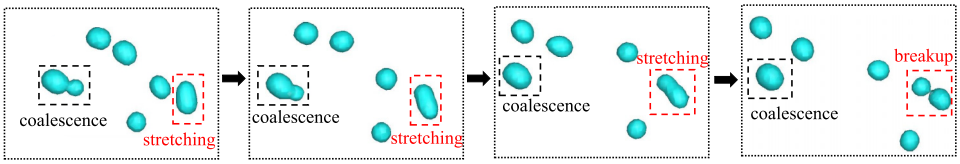

(a) t=t_0 (b) t=t_0+1/12T (c) t=t_0+1/6T (d) t=t_0+1/4T

FIG. 5. The bubble coalescence and breakup behaviors in the wake at $Q_v = 0.25$. T is the cycle of vortex shedding.

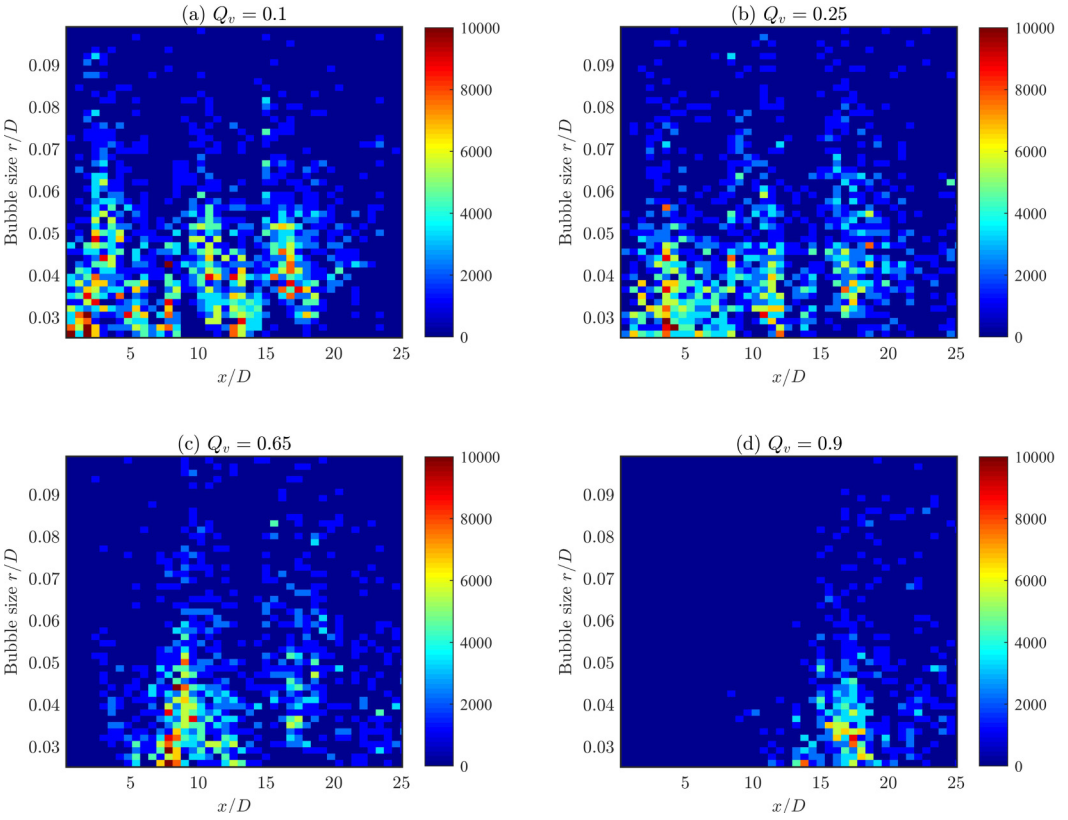

FIG. 6. The bubble number density distribution of bubble radius r/D versus the downstream locations x/D in the wake for four different values of the gas entrainment coefficient Q_v. The color represents the bubble number density.

coalescence process, the bubbles simultaneously approach together and merge into a large bubble. In terms of breakup process, the bubble stretches and when it reaches a certain extent, it breaks into two small bubbles. With the further increase in Q_v [Fig. 4(c)], the upper part of the cavity is filled with gas, and there is a clear cavity interface. The re-entrant jet becomes weaker, and it can no longer penetrate forward to reach the cylinder. The peak value position of bubble number moves downstream (shown in Fig. 6). At $Q_v = 0.9$ [Fig. 4(d)], most of the gas forms a transparent cavity. Both the upper and lower cavity surfaces are relatively smooth and glassy. Some gas moves along the cavity interface, and, in the closure region, it mixes with liquid to form small-scale bubbles.

To investigate the influence of Q_v on the bubble statistics, the bubble number N, bubble Sauter mean diameter size D_{32}, and normalized bubble number N_d distribution in the domain are displayed in Figs. 7 and 8. Here, N_d is normalized by the bubble number N, and D_{32} is calculated as

$$D_{32} = \sum_{i=1}^{N} d_i^3 \Big/ \sum_{i=1}^{N} d_i^2, \tag{10}$$

where d_i is the diameter of a bubble and N is the total bubble number.

Figure 7 indicates that the Q_v plays an important role in determining the bubble number and bubble size. The changes in N and D_{32} in the wake of a cylinder are closely related to the events of bubble breakup and coalescence. With an increase in Q_v, the total bubble number N decreases. The normalized distribution of bubble number and the corresponding cumulative probability distribution

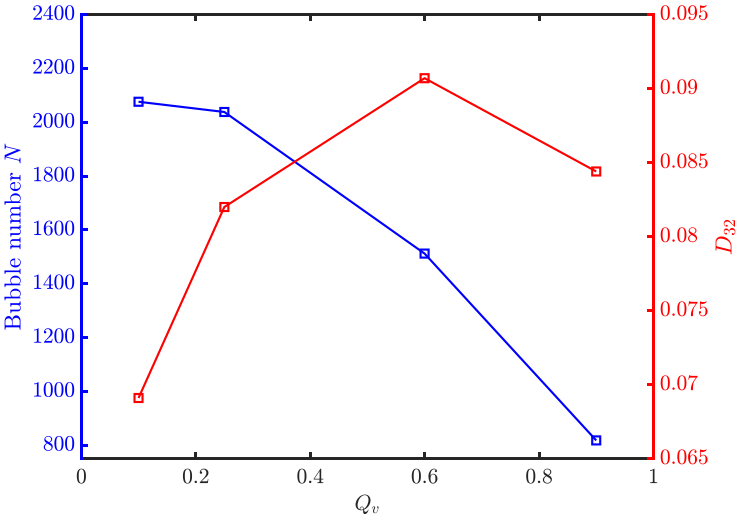

FIG. 7. Number of bubbles N and Sauter mean bubble diameter D_{32} for different values of the gas entrainment coefficient Q_v.

function are displayed in Fig. 8. It can be seen that the bubble size distribution has a universally similar shape for different values of Q_v. Karn *et al.* [50] demonstrated that changes in the air ventilation rate did not affect the width of the distribution at a fixed liquid velocity. As shown in Fig. 7, the bubble distribution can be divided into three regions with two critical values of bubble diameter r_1 and r_2. In region I ($r_i < r_1$), with increasing bubble size, the dimensionless bubble number increases. However, in region II ($r_1 < r_i < r_2$), the dimensionless bubble number starts decreasing. In region III ($r_i > r_2$), when the bubble size is greater than r_2, the dimensionless bubble number remains almost zero and there are very few bubbles.

B. Vortex structures in the wake

In order to present the effects of developed ventilated cavitation on the vortex structures, side view and perspective view of instantaneous vortex structures educed using the Q criterion [51] with the isosurface $Q = 0.8$ and colored by the spanwise vorticity ω_z ($\omega_z = \partial v/\partial x - \partial u/\partial y$) values are displayed in Fig. 9. For the single phase flow ($Q_v = 0$), the upper separated shear layer rolls up, forming a clockwise vortex (CV1) with negative vorticity (blue), as shown in Fig. 9(a). For another clockwise vortex CV2 downstream, owing to its intense stretching, horseshoe vortex structures appear in the neck region of CV2. Consecutive vortices with opposite rotation directions are connected by the streamwise ribs (R1). The alternately shed vortices form a vortex street. When gas is injected into the flow, a cavity attached to the cylinder is formed. For $Q_v = 0.1$, the vortex structures in the wake behave similar to those in the single phase flow. The difference is that the location of vortex shedding moves downstream, and the vortices are deformed. When Q_v is increased to 0.25, some small-scale vortices are found below the cavity interface. These small-scale vortices are caused by the deformation and propagation of the cavity interface [52]. Meanwhile, in the lower part, the re-entrant jet penetrates forward to the back of the cylinder. The shear layer with positive vorticity rolls up, forms large-scale vortices, and propagates downstream. Compared with the large-scale vortex structures for $Q_v = 0.1$, the vortices are less regular in shape and more stretched for $Q_v = 0.25$. With increasing Q_v ($Q_v = 0.65$), the length of the cavity increases further, and a relatively smooth cavity interface is formed in the upper part. In the lower part, the re-entrant jet impinges on the cavity interface to make it rough, unsteady, and opaque, accompanied by vortices of various sizes. At the rear of the cavity, the instability of the cavity interface and the re-entrant jet

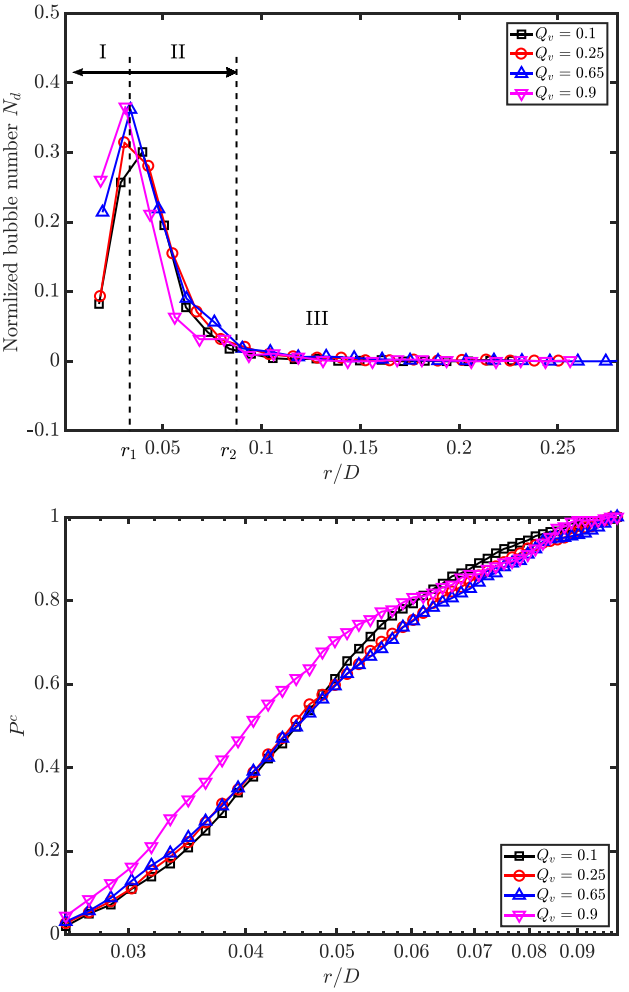

FIG. 8. (Top panel) Normalized distribution of bubble number in the domain. (Bottom panel) The cumulative probability distribution function (cpdf) for different values of the gas entrainment coefficient Q_v.

promote large-scale vortex shedding. For $Q_v = 0.9$, the re-entrant jet is suppressed and the region near the bluff body is fully filled by air and the cavity interface has a transparent appearance.

For the single phase flow, the boundary layers on the cylinder separate due to the adverse pressure gradient, forming the shear layers. Then the two shear layers with opposite signs alternately roll up and are shed into the wake to form the vortex street [53]. The characteristics of vortex shedding are determined by the combined effect of the shear layer strength and the formation region size [54]. In the ventilated cavitating flow, the vortex shedding structures are altered. To gain insight into the vortex shedding mechanism in the ventilated cavitating flow, the instantaneous spanwise vorticity ω_z in the midplane at different Q_v are depicted in Fig. 10. At $Q_v = 0$ and $Q_v = 0.1$, the vortex formation processes do not have significant difference. In both cases, the vortices are produced by rolling up and shedding the shear layer from the circular cylinder. However, when the gas entrainment coefficient reaches $Q_v = 0.65$, a large cavity with glassy surface forms. The position of cavitation separation is different from the position of boundary-layer separation [55]. As a result, there exist two shear layers with negative vorticity along the upper cavity surface. One shear layer [shear layer 1 in Fig. 10(d)] develops from the surface of the cylinder, and the other shear layer (shear layer

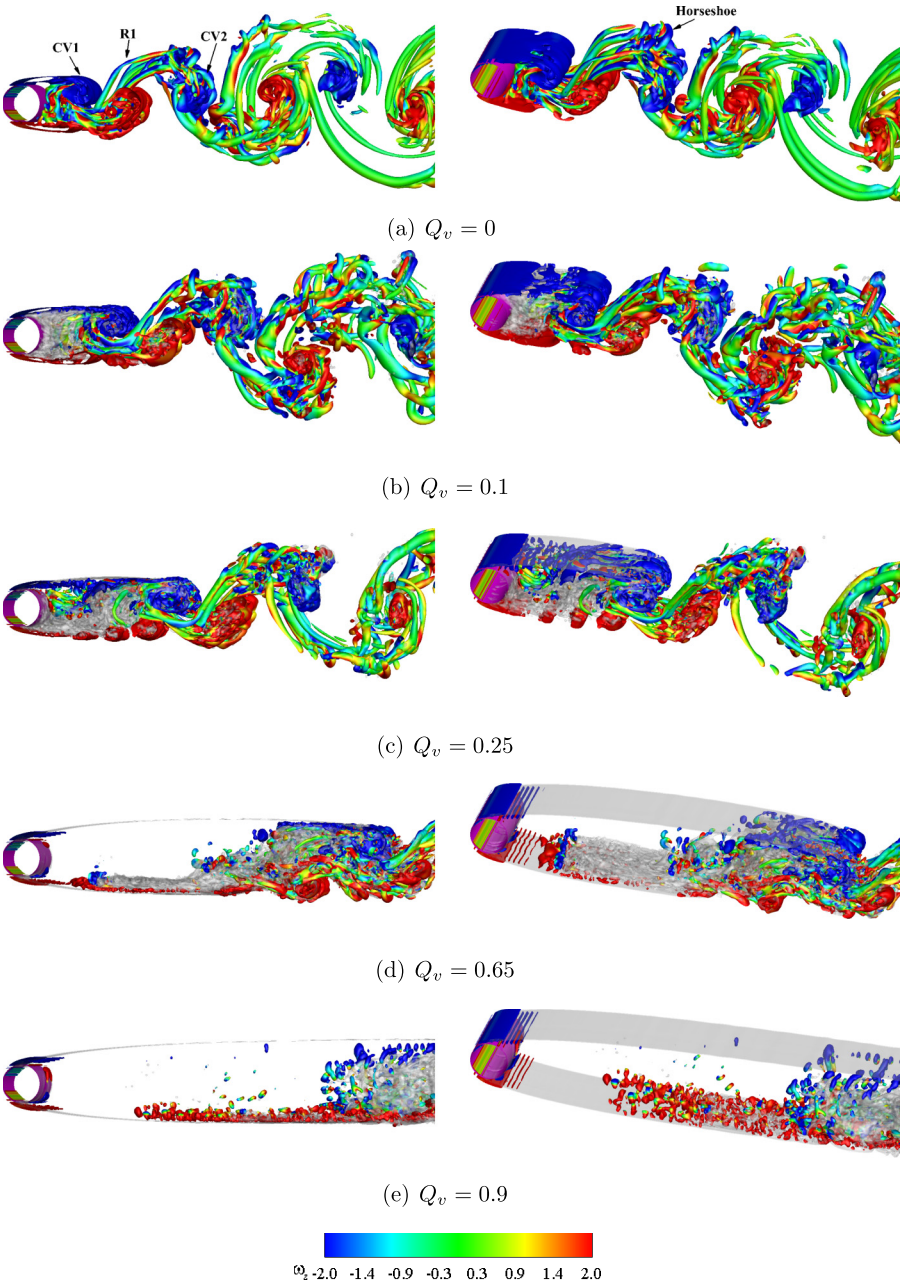

FIG. 9. Flow vortex structures at Re = 1000 visualized with isosurface of Q criterion ($Q = 0.8$) colored by the spanwise vorticity ω_z in side view (left) and perspective view (right): (a) $Q_v = 0$, (b) $Q_v = 0.1$, (c) $Q_v = 0.25$, (d) $Q_v = 0.65$, (e) $Q_v = 0.9$. Isocontour of gas volume fraction $\alpha_g = 0.5$ is displayed in gray.

2) forms from the cavity surface. The cavity surface prevents the rollup of shear layer 1. At the closure region, shear layer 1 attaches to the cavity surface and joins shear layer 2 to form the closed recirculation region. Then the shear layers in the upper and bottom sides interact at the closure region, delaying the vortex shedding. In the cavity, a re-entrant jet occurs due to the adverse pressure

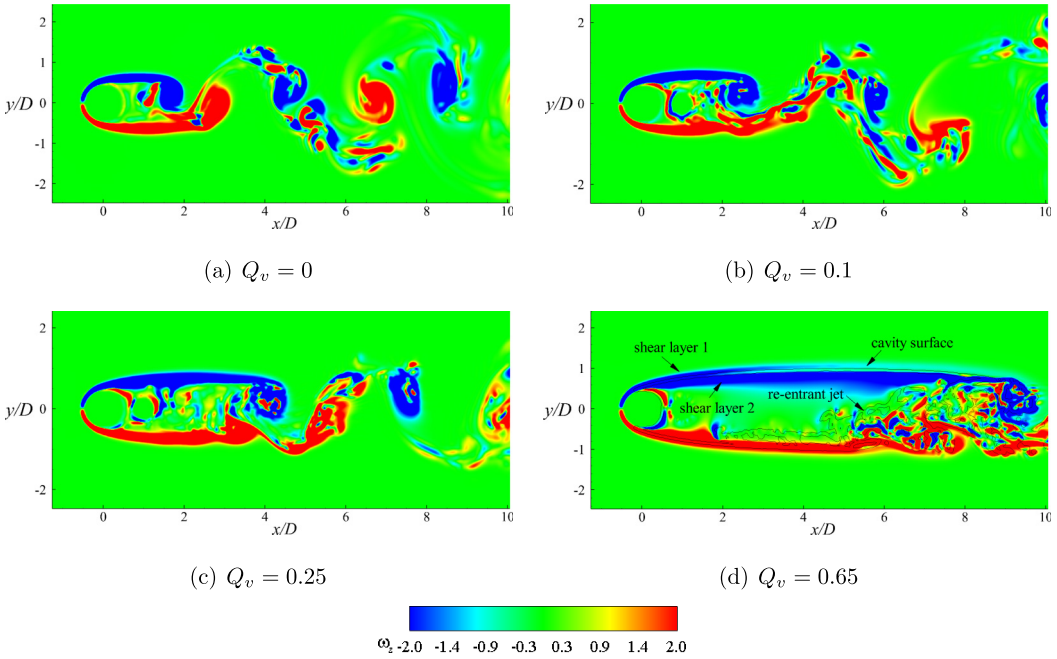

FIG. 10. Instantaneous spanwise vorticity ω_z at different gas entrainment coefficient (a) $Q_v = 0$, (b) $Q_v = 0.1$, (c) $Q_v = 0.25$, (d) $Q_v = 0.65$. The black line in panel (d) represents the cavity surface.

gradient in the closure region. The development of re-entrant jet, the instability of cavity surface, and the separation of shear layer 1 jointly lead to the vortex formation and shedding. In this case, the separation of shear layers from the surface of the cylinder is no longer the main factor of vortex shedding.

To reveal the effect of ventilated cavitation on the vortex shedding processes described above, time evolution of streamwise velocity u/U at representative positions for different gas entrainment coefficient Q_v values are depicted in Fig. 12. The locations of these points are as follows: $P1$ $(x/D = 0.175, y/D = 0.625)$, $P2$ $(x/D = 1.475, y/D = 0.35)$, $P3$ $(x/D = 3.475, y/D = 0.725)$, $P4$ $(x/D = 4.1, y/D = 0)$, as shown in Fig. 11. For $P1$, it is located at the shear layer for all cases. One can notice similar sinusoidal-like fluctuations in the cases $Q_v = 0$ and $Q_v = 0.1$. The difference between theses two cases lies in the fluctuation amplitude and period. It is worthwhile to note that the velocity fluctuation gradually decays and tends to become more stable with the increase of

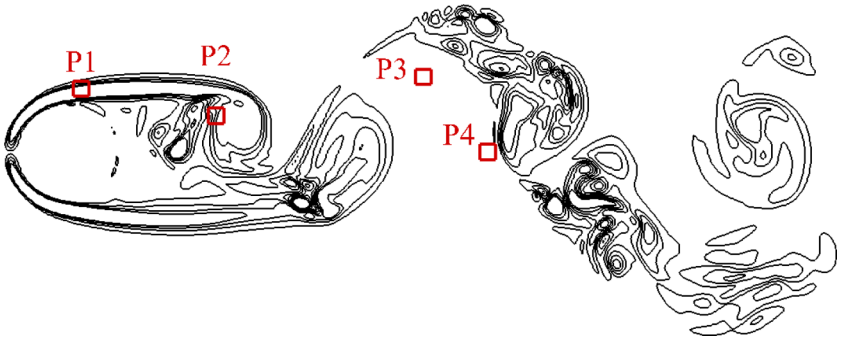

FIG. 11. The location of monitoring points.

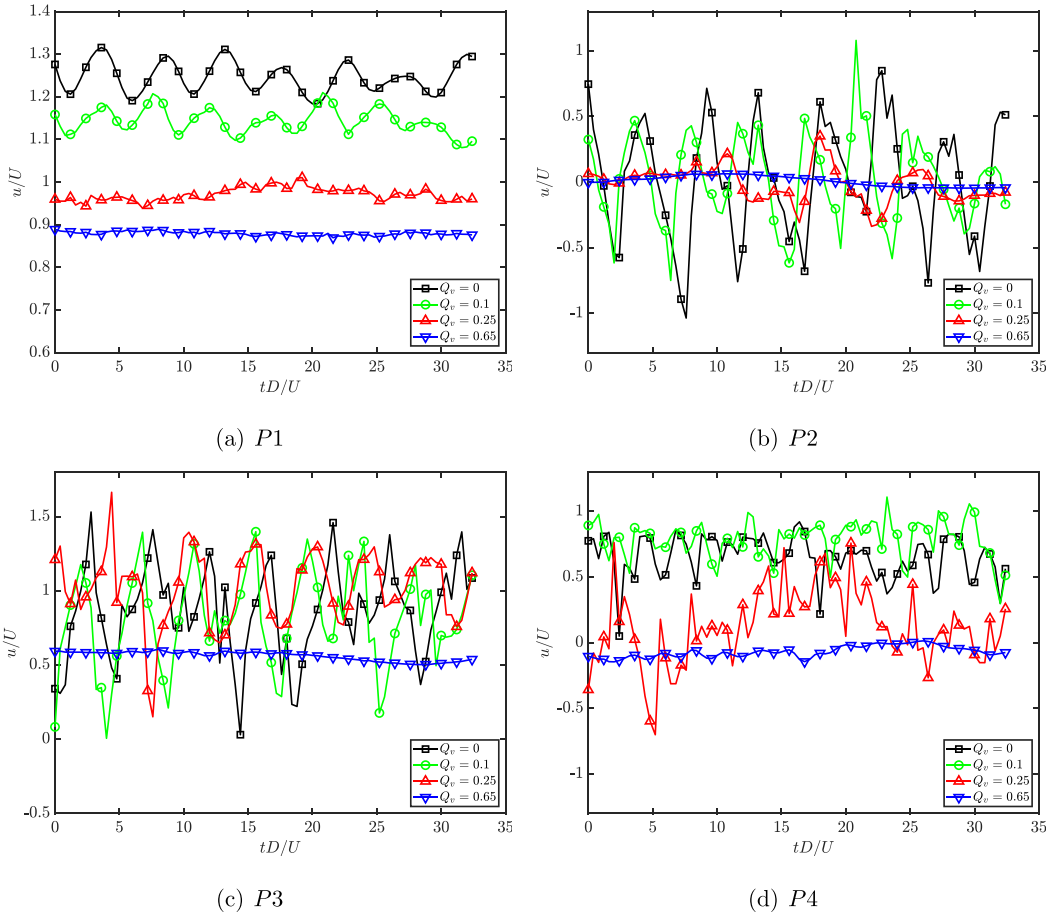

FIG. 12. Time history of the streamwise velocity for different Q_v at locations: (a) $P1$, (b) $P2$, (c) $P3$, (d) $P4$.

Q_v, which indicates that the ventilated cavitation alters the local stability of the flow due to the effect of the cavity surface on the shear layer detached from the cylinder. For the cases $Q_v = 0$ and $Q_v = 0.1$, the point $P2$ is near the vortex shedding region. The velocity curves fluctuate up and down. For the other two cases, $Q_v = 0.25$ and $Q_v = 0.65$, this point $P2$ is located in the cavity. Due to the development of the re-entrant jet, the velocity begins to oscillate. However, at $Q_v = 0.65$, the strength of the re-entrant jet becomes weakened and its effect is mild. As a result, the value of streamwise velocity almost keeps zero. At $P3$, the streamwise velocity curves show fluctuations due to the vortex shedding for the first three cases, $Q_v = 0$, 0.1, and 0.25. At $Q_v = 0.65$, the flow becomes supercavitation, which has three characteristic regions in the cavity: a ventilation region, a high shear region (internal boundary layer), and a reverse flow region [56]. The internal boundary layer was identified as the region between the location of zero velocity and the cavity interface. For $P3$, it is located inside the internal boundary layer of the ventilated cavitation and the value of velocity there is nearly $0.55U$. No trace of velocity fluctuations is found in these cases. The point of $P4$ is set in the wake centerline. For $Q_v = 0$ and $Q_v = 0.1$, this point is in the wake after vortex shedding. The shedding vortices pass through this point, and the amplitude of velocity fluctuations at $P4$ decreases. For $Q_v = 0.25$, the velocity variation caused by the effect of both re-entrant jet and the vortex shedding. For $Q_v = 0.65$, $P4$ is in the reverse flow region and thus the velocity denotes the motion of re-entrant jet flow. It can be further found that the velocity of re-entrant jet is nearly

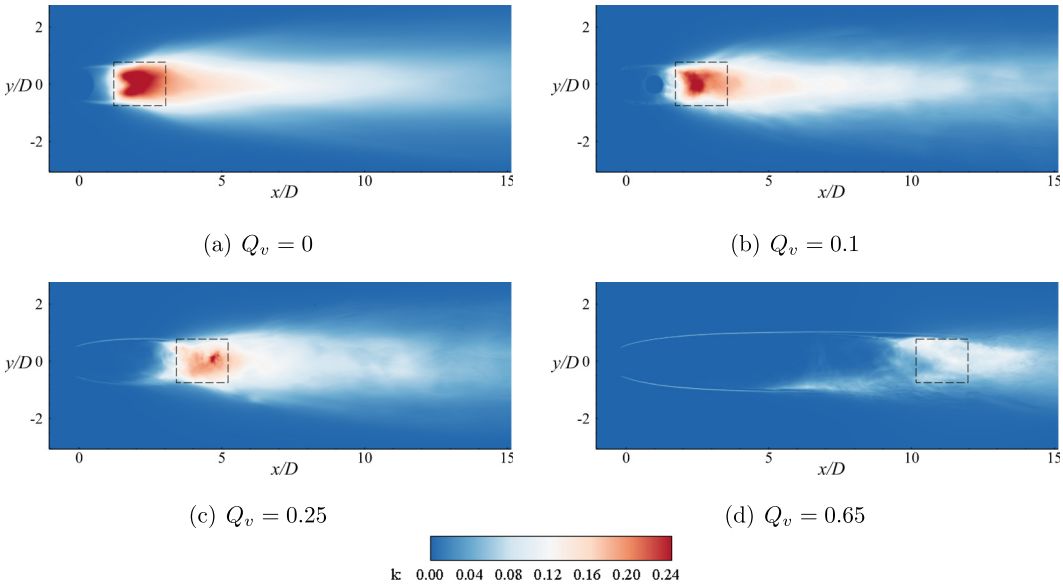

FIG. 13. Contours of turbulent kinetic energy distribution for cases with different values of Q_v. The region of black dotted rectangle represents the closure region.

constant. As discussed by Callenaere [16], the velocity of the re-entrant jet stays constant all along its development.

C. Turbulent kinetic energy

Figure 13 displays the distribution of turbulent kinetic energy (TKE) for different values of Q_v. For all cases, the TKE is mainly distributed in the closure region (the black dotted rectangle in Fig. 13). The high turbulence intensity in the closure region could also explain the trend of bubble number variation in Fig. 6, as well as providing further evidence that both bubble breakup and coalescence are related to the turbulence intensity. For single phase flow ($Q_v = 0$), the TKE reaches its peak value near the saddle point and then decreases as the downstream distance increases. From a comparison of the TKE at $Q_v = 0$ with that at $Q_v = 0.1$, we can see that the distributions are similar. This indicates that the flow structures are still dominated by the single phase flow. When Q_v is increased to 0.25, the location of the TKE peak value moves downstream and the value decreases. This suggests that the development of ventilated cavitation suppresses both the rollup of the shear layer and the vortex shedding. For $Q_v = 0.65$, the front of the cavity is transparent and the TKE is small, showing a stable state.

D. Vortex dynamics in the wake

As presented in Subsec. B, the ventilated cavitation plays an important role in the vortex structures. To explain this phenomenon, the enstrophy ω^2 ($\omega^2 = \omega_x^2 + \omega_y^2 + \omega_z^2$) distribution and the enstrophy transport are investigated in this section. As can be seen in Fig. 14, the enstrophy ω^2 is mainly concentrated in the shear layer region (I) and the closure region for $Q_v = 0$. When gas is injected into the flow, with $Q_v = 0.1$, the enstrophy distribution is similar to that for $Q_v = 0$. However, the strength of the enstrophy increases owing to the interaction between water and gas. For Q_v =0.25, the enstrophy also distributes in the re-entrant jet region (III). With further increase in Q_v to 0.65, a clear cavity interface emerges, and the enstrophy distribution changes significantly. It is distributed not only in the shear layer region (I) and the closure region (II), but also in the

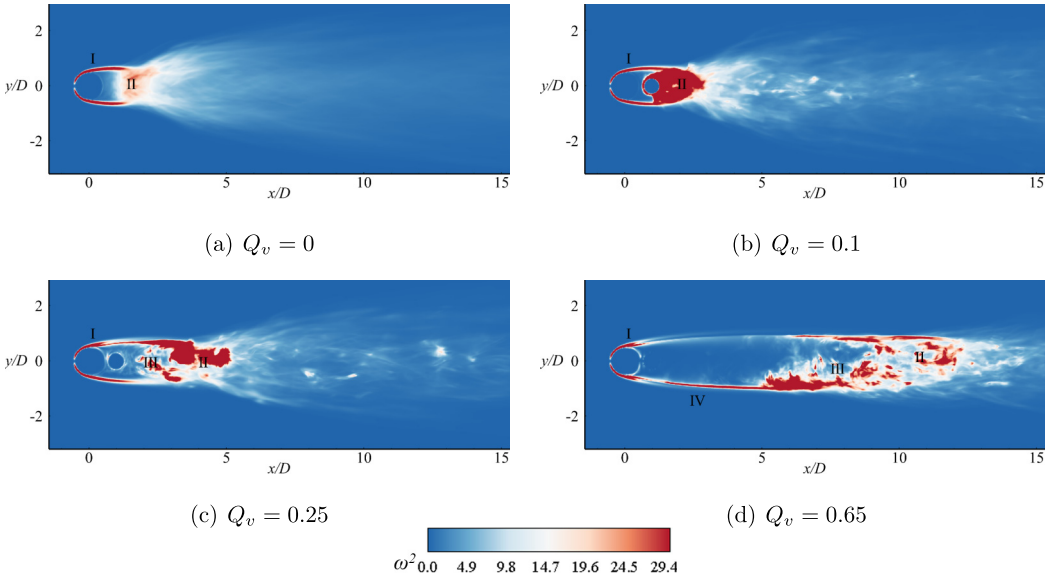

(a) $Q_v = 0$ (b) $Q_v = 0.1$ (c) $Q_v = 0.25$ (d) $Q_v = 0.65$

FIG. 14. Contours of enstrophy ω^2 for different values of the gas entrainment coefficient Q_v. The regimes I, II, III, and IV represent shear layer region, closure region, re-entrant region, and cavity interface region, respectively.

re-entrant jet region (III) and the cavity interface (IV). This indicates that the existence of re-entrant jet flow and the instability of the cavity interface are also the reasons for the formation of vortices.

To show the mechanism of vortex generation and balance in ventilated cavitating flow, we consider the vorticity enstrophy transport equation [57–60]

$$\frac{\partial}{\partial t}\left(\frac{1}{2}\omega_i\omega_i\right) + u_j\frac{\partial}{\partial x_j}\left(\frac{1}{2}\omega_i\omega_i\right) = \omega_i\omega_j\frac{\partial u_i}{\partial x_j} + \frac{1}{\rho^2}\omega_i\varepsilon_{ijk}\frac{\partial\rho}{\partial x_j}\frac{\partial p}{\partial x_k} + \omega_i\varepsilon_{ijk}\left(\frac{1}{\rho}\frac{\partial\tau_{km}}{\partial x_k}\right). \tag{11}$$

The first term on the right-hand side of the equation above is the stretching term $W_s = \omega_i\omega_j\partial u_i/\partial x_j$, the second term is the baroclinic term $W_b = \rho^{-2}\omega_i\varepsilon_{ijk}(\partial\rho/\partial x_j)(\partial p/\partial x_k)$, and the last term is the viscous term $W_v = \omega_i\varepsilon_{ijk}(\frac{1}{\rho}\frac{\partial\tau_{km}}{\partial x_k})$. In this study, the surface tension effects are assumed small and are neglected [15,61,62].

Figures 15, 16, and 17 display the contours of the stretching, baroclinic, and viscous terms, respectively, for cases with different Q_v. The stretching term (Fig. 15) has a positive contribution to the enstrophy transport and mainly concentrates on the closure region (II). Comparing with single phase flow $Q_v = 0$, the stretching term increases when the Q_v is relatively small ($Q_v = 0.1$). Examination of the effect of Q_v on the enstrophy transport shows that the stretching term decreases with increasing Q_v. This suggests that the development of ventilated cavitation has an inhibitory effect on the stretching and rotation of vortices.

For the baroclinic term (Fig. 16), the flow is single phase and the density is constant ($Q_v = 0$). Therefore, the baroclinic term is zero and does not influence the enstrophy transport [Fig. 16(a)]. For ventilated cavitating flows, the mixing of water and gas causes the density to vary, and the baroclinic term is no longer zero. The baroclinic term distributes in the closure region II and the re-entrant jet region III with a positive value, which results in an increase in enstrophy. These observations indicate that the baroclinic term acts as a significant source of enstrophy production for the ventilated cavitating flow.

From Fig. 17, it can be found that the viscous term is always negative for the dissipation of enstrophy. For the single phase flow ($Q_v = 0$), the enstrophy transport is principally determined by

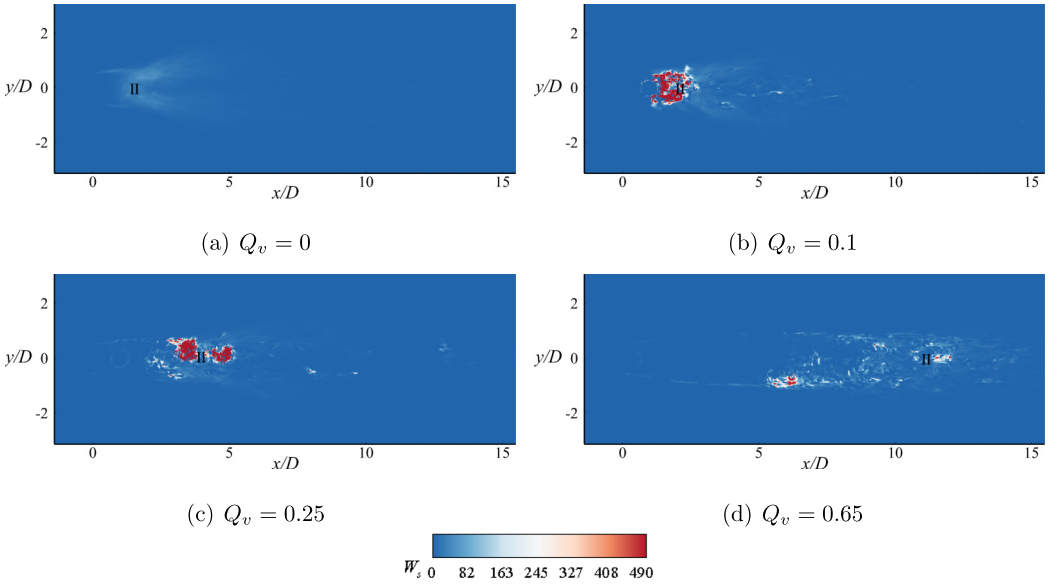

FIG. 15. Contours of the stretching term in the enstrophy equation for different values of Q_v.

the stretching and viscous terms. However, for ventilated cavitating flow, the distributions of the viscous term is similar to that of the baroclinic term, which indicates that the dissipation caused by the viscous term is mostly compensated by the baroclinic term. In addition, it indicates that the production of enstrophy in the closure region II and re-entrant jet region III is mainly contributed by the baroclinic term.

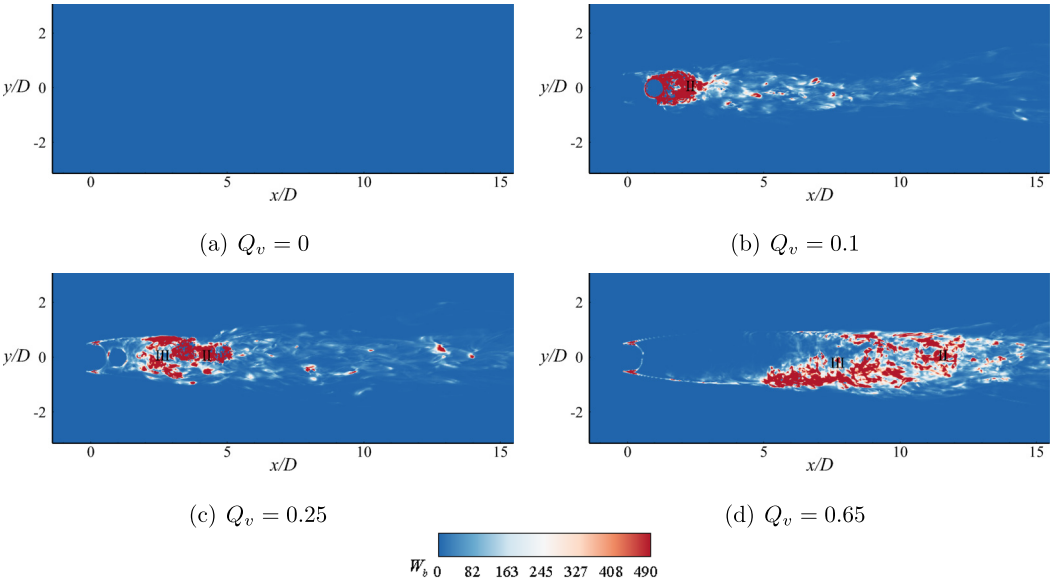

FIG. 16. Contours of the baroclinic term in the enstrophy equation for different values of Q_v.

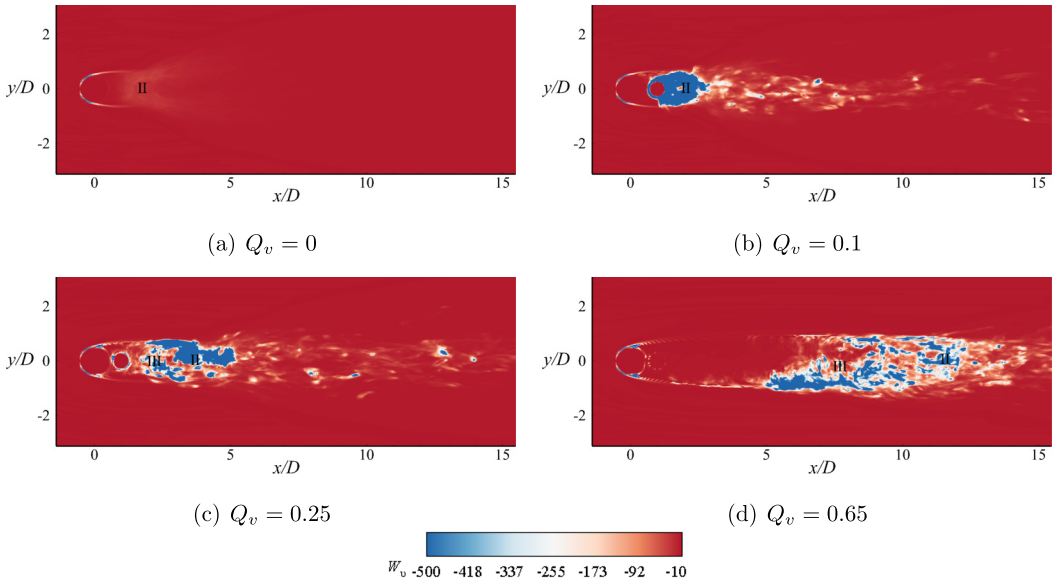

FIG. 17. Contours of the viscous term in the enstrophy equation for different values of Q_v.

V. CONCLUSIONS

In this study, the characteristics of ventilated cavitating flow in the wake over of a circular cylinder have been studied by numerical simulation. The primary findings are the following.

(1) The development of ventilated cavitation affects bubble behavior in the wake. With increasing gas entrainment coefficient Q_v, there is a significant reduction in turbulence intensity in the closure region, which leads to a decrease in bubble number and an increase in the Sauter mean diameter of the bubbles. However, the form of the dimensionless bubble diameter distribution is almost invariable.

(2) The development of ventilated cavitation plays an important role in formation of vortices in the wake. For $Q_v = 0$, the shear layer rolls up to form vortices. However, when a cavity interface forms for $Q_v = 0.65$, two stable shear layers become attached to the cylinder. At the rear part, vortex shedding mainly results from the instability of the cavity interface and the appearance of a re-entrant jet flow.

(3) The enstrophy distribution is used to analyze the dynamics of vortex intensity. In contrast to single-phase flow, the enstrophy of a ventilated cavity is distributed not only at the shear layer and in the closure region, but also at the cavity interface and in the re-entrant jet region. In addition, the analysis of enstrophy transport indicates that the re-entrant jet plays an important role in the generation of the vortices.

ACKNOWLEDGMENTS

Z.W., Z.W., and G.W. gratefully acknowledge the support by the National Natural Science Foundation of China (Grants No. 11902323 and No. 11772341), the Key Research Program of Frontier Science of the Chinese Academy of Science (Grant No. QYZDBSSW-SYS015), and the Strategic Priority Research Program of the Chinese Academy of Science (Grant No. XDB22040203). Z.W. also appreciates the support from the China Scholarship Council for her visit to the University of Minnesota in 2018–2019 to conduct this study.

[1] R. E. A. Arndt, Cavitation in vortical flows, Annu. Rev. Fluid Mech. **34**, 143 (2002)
[2] C. E. Brennen, *Cavitation and Bubble Dynamics* (Oxford University Press, Oxford, UK, 1995).
[3] D. Fuster, A review of models for bubble clusters in cavitating flows, Flow, Turbul. Combust. **102**, 497 (2019).
[4] J. P. Franc and J. M. Michel, Fundamentals of cavitation, Fluid Mech. Its Appl. **76**, 1 (2004).
[5] C. X. Jiang, S. L. Li, F. C. Li, and W. Y. Li, Numerical study on axisymmetric ventilated supercavitation in influenced by drag-reduction additives, Int. J. Heat Mass Trans. **115**, 62 (2017).
[6] S. J. Lee, E. Kawakami, and R. E. A. Arndt, Investigation of the behavior of ventilated supercavities in a periodic gust flow, J. Fluids Eng. **135**, 081301 (2013).
[7] M. Wonsnik and R. E. A. Arndt, Measurements in high void-fraction bubbly wakes created by ventilated supercavitation, J. Fluids Eng. **135**, 011304 (2013).
[8] Z. Y. Wang, B. Huang, G. Y. Wang, M. D. Zhang, and F. F. Wang, Experimental and numerical investigation of ventilated cavitating flow structures with special emphasis on gas leakage behavior and re-entrant jet dynamics, Ocean Eng. **108**, 191 (2015).
[9] A. Karn, R. E. A. Arndt, and J. R. Hong, An experimental investigation into supercavity closure mechanisms, J. Fluid Mech. **789**, 259 (2016).
[10] S. Y. Shao, A. Karn, B. K. Ahn, R. E. A. Arndt, and J. R. Hong, A comparative study of natural and ventilated supercavitation across two closed-wall water tunnel facilities, Exp. Therm. Fluid Sci. **88**, 519 (2017).
[11] P. F. Pelz, T. Keil, and T. F. Gros, The transition from sheet to cloud cavitation, J. Fluid Mech. **817**, 439 (2017).
[12] S. A. Makiharju, H. Ganesh, and S. L. Ceccio, The dynamics of partial cavity formation, shedding, and the influence of dissolved and injected non-condensable gas, J. Fluid Mech. **829**, 420 (2017).
[13] K. L. De Graaf, P. A. Brandner, and B. W. Pearce, Spectral content of cloud cavitation about a sphere, J. Fluid Mech. **812**, 1 (2017).
[14] Y. W. Wang, C. Xu, X. C. Wu, C. G. Huang, and X. Q. Wu,Ventilated cloud cavitating flow around a blunt body close to the free surface, Phys. Rev. Fluids **2**, 084303 (2017).
[15] B. Budich, S. J. Schmidt, and N. A. Adams, Numerical simulation and analysis of condensation shocks in cavitating flow, J. Fluid Mech. **838**, 759 (2018).
[16] M. Callenaere, J. Franc, J. Michel, and M. Riondet, The cavitation instability induced by the development of a re-entrant jet, J. Fluid Mech. **444**, 223 (2001).
[17] B. Ji, X. W. Luo, R. E. A. Arndt, X. X. Peng, and Y. L. Wu, Large eddy simulation and theoretical investigations of the transient cavitating vortical flow structure around a NACA66 hydrofoil, Int. J. Multiphase Flow **68**, 121 (2015).
[18] C. M. Harwood, Y. L. Young, and S. L. Ceccio, Ventilated cavities on a surface-piercing hydrofoil at moderate Froude numbers: Cavity formation, elimination, and stability, J. Fluid Mech. **800**, 5 (2016).
[19] P. Ausoni, M. Farhat, X. Escaler, E. Egusquiza, and F. Avellan, Cavitation influence on Kármán vortex shedding and induced hydrofoil vibrations, J. Fluids Eng. **129**, (2007).
[20] A. Gnanaskandan and K. Mahesh, Large eddy simulation of the transition from sheet to cloud cavitation over a wedge, Int. J. Multiphase Flow **83**, 86 (2016).
[21] P. Kumar, D. Chatterjee, and S. Bakshi, Experimental investigation of cavitating structures in the near wake of a cylinder, Int. J. Multiphase Flow **89**, 207 (2017).
[22] Z. Y. Wang, B. Huang, M. D. Zhang, G. Y. Wang, and X. A. Zhao, Experimental and numerical investigation of ventilated cavitating flow structures with special emphasis on vortex shedding dynamics, Int. J. Multiphase Flow **98**, 79 (2018).
[23] H. Haddadi, S. Shojaei-Zadeh, K. Connington, and J. F. Morris, Suspension flow past a cylinder: Particle interactions with recirculating wakes, J. Fluid Mech. **760**, R2 (2014).
[24] B. Kaoui, Flow and mass transfer around a core-shell reservoir, Phys. Rev. E **95**, 063310 (2017).
[25] C. Bielinski, N. Le, and B. Kaoui, Unsteady mass transfer from a core-shell cylinder in crossflow, Phys. Rev. Fluids **6**, 023501 (2021).

[26] V. K. Krastev, G. Amati, S. Succi, and G. Falcucci, On the effects of surface corrugation on the hydrodynamic performance of cylindrical rigid structures, Eur. Phys. J. E **41**, 95 (2018).
[27] B. Belahadji, J. Franc, and J. Michel, Cavitation in the rotational structures of a turbulent wake, J. Fluid Mech. **287**, 383 (1995).
[28] P. A. Brandner, G. J. Walker, P. N. Niekamp, and B. Anderson, An experimental investigation of cloud cavitation about a sphere, J. Fluid Mech. **656**, 147 (2010).
[29] A. Gnanaskandan and K. Mahesh, Numerical investigation of near-wake characteristics of cavitating flow over a circular cylinder, J. Fluid Mech. **790**, 453 (2016).
[30] M. P. Kinzel, J. W. Lindau, and R. F. Kunz, Air entrainment mechanisms from artificial supercavities: Insight based on numerical simulations, in *Proceedings of the 7th International Symposium on Cavitation*, Vol. 136 (Ann Arbor, MI, 2009).
[31] C. W. Hirt and B. D. Nichols, Volume of fluid (VOF) method for the dynamics of free boundaries, J. Comput. Phys. **39**, 201 (1981).
[32] A. Russo, M. Icardi, M. Elsharkawy, D. Ceglia, P. Asinari, and C. M. Megaridis, Numerical simulation of droplet impact on wettability-patterned surfaces, Phys. Rev. Fluid **5**, 074002 (2020).
[33] M. Sussman, S. Peter, and O. Stanley, A level set approach for computing solutions to incompressible two-phase ow, J. Comput. Phys. **114**, 146 (1994).
[34] M. Sussman and E. G. Puckett, A coupled level set and volume-of-fluid method for computing 3D and axisymmetric incompressible two-phase flows, J. Comput. Phys. **162**, 301 (2000).
[35] J. Kim and J. S. Lee, Numerical study of cloud cavitation effects on hydrophobic hydrofoils, Int. J. Heat Mass Transf. **83**, 591 (2015).
[36] M.-R. Pendar and E. Roohi, Cavitation characteristics around a sphere: An LES investigation, Int. J. Multiphase Flow **98**, 1 (2018).
[37] D. L. Sun and W. Q. Tao, A coupled volume-of-fluid and level set VOSET method for computing incompressible two-phase flows, Int. J. Heat Mass Transf. **53**, 645 (2010).
[38] N. K. Singh and B. Premachandran, A two-dimensional numerical study of film boiling over an elliptical cylinder in the mixed regime under aiding and orthogonal saturated liquid flow configurations, J. Fluid Mech. **908**, A44 (2021).
[39] Z. X. Yang, X. H. Lu, X. Guo, Y. Liu, and L. Shen, Numerical simulation of sediment suspension and transport under plunging breaking waves, Comput. Fluids **158**, 57 (2017).
[40] Z. X. Yang, B. Q. Deng, and L. Shen, Direct numerical simulation of wind turbulence over breaking waves, J. Fluid Mech. **85**, 120 (2018).
[41] J. Kim and P. Moin, Application of a fractional-step method to incompressible Navier-Stokes equations, J. Comput. Phys. **59**, 308 (1985).
[42] H. Liu, Z. Xiao, and L. Shen, Simulation based study of supercavitation turbulence, in *Proc. of the 10th International Workshop on Ship and Marine Hydrodynamics, Keelung, Taiwan, China* (2017).
[43] D. Zi, A. Xuan, F. Wang, and L. Shen, Numerical study of mechanisms of air-core vortex evolution in an intake flow, Int. J. Heat Fluid Flow **81**, 108517 (2020).
[44] J. Yang and E. Balaras, An embedded-boundary formulation for large-eddy simulation of turbulent flows interacting with moving boundaries, J. Comput. Phys. **215**, 12 (2006).
[45] A. Calderer, X. Guo, L. Shen, and F. Sotiropoulos, Fluid-structure interaction simulation of floating structures interacting with complex, large-scale ocean waves and atmospheric turbulence with application to floating offshore wind turbines, J. Comput. Phys. **355**, 144 (2018).
[46] Z. Cui, Z. X. Yang, H. Z. Jiang, W. X. Huang, and L. Shen, A sharp-interface immersed boundary method for simulating incompressible flows with arbitrarily deforming smooth boundaries, Int. J. Comp. Methods **15**, 1750080 (2018).
[47] O. Coutier-Delgosha, J. F. Devillers, T. Pichon, A. Vabre, and S. Legoupil, Internal structure and dynamics of sheet cavitation, Phys. Fluids **18**, 263 (2006).
[48] M. Herrmann, A parallel Eulerian interface tracking/Lagrangian point particle multi-scale coupling procedure, J. Comput. Phys. **229**, 745 (2010).
[49] Q. Gao, G. B. Deane, H. Liu, and L. Shen, A robust and accurate technique for Lagrangian tracking of bubbles and detecting fragmentation and coalescence, Int. J. Multiphase Flow **135**, 103523 (2021).

[50] A. Karn, S. Y. Shao, R. E. A. Arndt, and J. Hong, Bubble coalescence and breakup in turbulent bubbly wake of a ventilated hydrofoil, Exp. Thermal Fluid Sci. **70**, 397 (2016).
[51] J. C. Hunt, A. A. Wray, and P. Moin, Eddies, streams, and convergence zones in turbulent flows, in *Center for Turbulence Research Report CTR-S88* (1988).
[52] M. S. Longuet-Higgins, Capillary rollers and bores, J. Fluid Mech. **240**, 659 (1992).
[53] E. A. Anderson and A. A. Szewczyk, Effects of a splitter plate on the near wake of a circular cylinder in two- and three-dimensional flow congurations, Exp. Fluids **23**, 161 (1997).
[54] J. H. Gerrard, The mechanics of the formation region of vortices behind bluff bodies, J. Fluid Mech. **25**, 401 (1966).
[55] V. H. Arakeri, Viscous effects on the position of cavitation separation from smooth bodies, J. Fluid Mech. **68**, 779 (1975).
[56] Y. Wu, Y. Liu, S. Shao, and J. Hong, On the internal flow of a ventilated supercavity, J. Fluid Mech. **862**, 1135 (2019).
[57] M. Brøns, M. C. Thompson, T. Leweke, and K. Hourigan, Vorticity generation and conservation for two-dimensional interfaces and boundaries, J. Fluid Mech. **758**, 63 (2014).
[58] J. Z. Wu, A theory of three-dimensional interfacial vorticity dynamics, Phys. Fluids **7**, 2375 (1995).
[59] A. Kazbekov, K. Kumashiro, and A. M. Steinberg, Enstrophy transport in swirl combustion, J. Fluid Mech. **876**, 715 (2019).
[60] Z. Zhao, N. S. Liu, and X. Y. Lu, Kinetic energy and enstrophy transfer in compressible Rayleigh-Taylor turbulence, J. Fluid Mech. **904**, A37 (2020).
[61] M. Bhatt and K. Mahesh, Numerical investigation of partial cavitation regimes over a wedge using large eddy simulation, Int. J. Multiphase Flow **122**, 103155 (2019).
[62] F. L. Brandao, M. Bhatt, and K. Mahesh, Numerical study of cavitation regimes in flow over a circular cylinder, J. Fluid Mech. **885**, A19 (2020).